University of Groningen

Analysis of banded morphology in multiphase steels based on a discrete dislocation-transformation model

Shi, Jingyi; Turteltaub, Sergio; van der Giessen, Erik

IMPORTANT NOTE: You are advised to consult the publisher's version (publisher's PDF) if you wish to cite from it. Please check the document version below.

Document Version
Publisher's PDF, also known as Version of record

Publication date:
2011

Link to publication in University of Groningen/UMCG research database

Analysis of banded morphology in multiphase steels based on a discrete dislocation–transformation model

Jingyi Shi[1]**, Sergio Turteltaub**[2] **and Erik Van der Giessen**[3]

[1] Huisman Equipment BV, Admiraal Trompstraat 2, 3115 HH Schiedam, The Netherlands
[2] Faculty of Aerospace Engineering, Delft University of Technology, Kluyverweg 1, 2629 HS Delft, The Netherlands
[3] Zernike Institute for Advanced Materials, University of Groningen, Nijenborgh 4, 9747 AG Groningen, The Netherlands

E-mail: s.r.turteltaub@tudelft.nl and E.van.der.Giessen@rug.nl

Abstract

The influence of the austenitic microstructural morphology on the mechanical response of a multiphase steel is analyzed by comparing two relevant configurations, namely (i) uniformly distributed grains of retained austenite embedded in a ferritic matrix and (ii) a banded morphology of the two phases. The analysis is carried out numerically using a discrete dislocation–transformation model that captures processes occurring at sub-grain length scales connected to nucleation and evolution of individual dislocations and martensitic platelets inside the austenitic grains. The simulations indicate that a microstructure composed of uniformly distributed grains of austenite is optimal in terms of strength since it delays the onset of plastic localization compared with banded microstructures.

1. Introduction

The microstructure of a typical high-strength low-alloyed multiphase steel assisted by transformation-induced plasticity, known as TRIP steels, consists of ferrite (dominant phase), bainite (composed of ferrite and cementite) and austenite (with volume fractions typically ranging from 5 to 20%) [1]. The presence of austenite, which has been retained in the microstructure upon cooling to room temperature, plays a critical role in this class of materials. Indeed, during deformation, whether in forming or during operation, the retained austenite transforms into a harder phase—martensite—providing this material with enhanced work-hardening characteristics. The effective (macroscopic) mechanical properties of TRIP steels strongly depend on the details of the microstructure, including grain size, volume fractions and grain distribution. Depending on the thermomechanical processing route and the addition of alloying elements, different microstructural morphologies can be generated for multiphase

steels [2, 3]. The influence of the *grain size* on the overall strength has been recently analyzed in [4] where it was found that the Hall–Petch effect becomes more relevant than the strengthening due to martensitic transformation as the ferritic and austenitic grain sizes decrease in samples of equal composition.

This work focuses on analyzing the influence of the spatial grain *distribution* on the response of a multiphase steel assisted by transformation-induced plasticity. In particular, two technologically important morphologies are analyzed, namely (i) a microstructure composed of *uniformly distributed* isolated grains of retained austenite and (ii) a banded microstructure composed of *continuous layers* of austenite and a ferritic matrix. The first configuration is representative of a typical TRIP steel that is cold-rolled and subsequently annealed in two steps (intercritical annealing followed by a second isothermal heat treatment). In the final microstructure, the retained austenite appears as isolated grains surrounded by a ferritic matrix. The second configuration is meant to mimic a banded morphology that sometimes appears as a consequence of mechanical deformation during processing (e.g. hot-rolling) which is not completely removed through further thermal treatment. The relevance of banded morphologies in ferrous alloys has been discussed in [5–7].

The manufacturing of materials with distinct morphologies involves different deformation and heat treatments that simultaneously affect a large number of microstructural parameters such as grain size, carbon content or crystal orientations. All the aforementioned parameters have an influence on the overall strength of a material, so that the differences in experimentally measured strengths of various morphologies cannot uniquely be ascribed to the different spatial distributions of grains. One advantage of numerical simulations is that the microstructural characteristics can be easily controlled, thus allowing for a direct comparison of the influence of morphologies whose only difference lies on grain distribution. To this end, the typical microstructure of a TRIP steel with uniformly dispersed austenitic grains is chosen as a reference while a banded microstructure is constructed as an alternative configuration such that only the spatial distribution of grains is modified while all the other microstructural parameters are kept the same.

Plastic deformation is modeled using a discrete dislocation model while phase transformations are accounted for by a discrete transformation model. This modeling approach, initiated in [4], allows to capture complex sub-grain interactions between dislocations and phase transformation that are difficult to describe using continuum constitutive models. Computational cells with various morphologies are used in simulations with periodic boundary conditions to mimic the bulk properties of the material and, thus, to determine the effective strength associated to the various microstructural configurations.

2. Discrete dislocation–transformation model for multiphase steels

The behavior of a discrete aggregate of ferritic (body-centered cubic—bcc) and austenitic (face-centered cubic—fcc) grains that may transform into martensitic platelets (twinned body-centered tetragonal—bct) is simulated using the discrete dislocation–transformation model presented in [4, 8], which is summarized in this section. The problem is decomposed into three sub-problems, namely (i) a martensitic transformation problem (platelets of martensite embedded in an infinite austenitic medium), (ii) the dislocation problem (dislocations embedded in an infinite medium, either ferrite or austenite) and (iii) a complementary problem, which accounts for a non-homogeneous, finite computational domain. The problems are shown schematically in figure 1. Correspondingly, the stress σ, strain ε and displacement u are
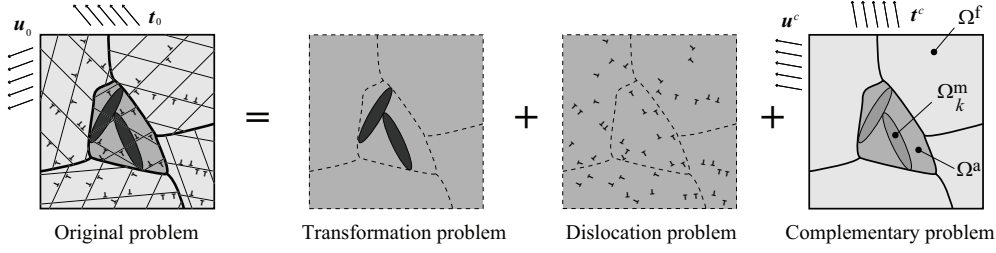
Figure 1. Schematic decomposition of the original dislocation–transformation problem into three sub-problems for an aggregate of grains of ferrite (Ω^f), austenite (Ω^a) and platelets of martensite (Ω_k^m).

decomposed as follows:

$$\boldsymbol{\sigma} = \boldsymbol{\sigma}^m + \boldsymbol{\sigma}^d + \boldsymbol{\sigma}^c, \qquad \boldsymbol{\varepsilon} = \boldsymbol{\varepsilon}^m + \boldsymbol{\varepsilon}^d + \boldsymbol{\varepsilon}^c, \qquad \boldsymbol{u} = \boldsymbol{u}^m + \boldsymbol{u}^d + \boldsymbol{u}^c, \qquad (1)$$

where the superscripts m, d and c refer to the martensitic transformation problem, the dislocation problem and the complementary problem, respectively. The fields for the transformation and dislocation problems are obtained analytically upon adding the individual solutions $\boldsymbol{\sigma}_k^m$, ε_k^m and $\boldsymbol{u}_k^m$ of each martensitic platelet $k = 1, \ldots, N^m$ and the solutions σ_i^d, ε_i^d and $\boldsymbol{u}_i^d$ for each dislocation $i = 1, \ldots, N^d$ in the domain (see [4] and [8]). The transformation fields $\boldsymbol{\sigma}_k^m$ and ε_k^m corresponding to a martensitic platelet k and the dislocation fields $\boldsymbol{\sigma}_i^d$ and ε_i^d connected to a dislocation i are constitutively related as

$$\boldsymbol{\sigma}_k^m = \begin{cases} \mathbb{C}^a \varepsilon_k^m & \text{in } \Omega - \Omega_k^m , \\ \mathbb{C}^m \left(\varepsilon_k^m - \varepsilon_k^{tr} \right) & \text{in } \Omega_k^m, \end{cases} \qquad (2)$$

and

$$\boldsymbol{\sigma}_i^d = \mathbb{C}^p \varepsilon_i^d \qquad \text{for } i \in \mathcal{A}^p , \ p = \text{f, a, m}, \qquad (3)$$

where the index $p = $ f, a, m refers to the ferritic, austenitic or martensitic phase, $\mathbb{C}^p$ is the tensor of elastic moduli of a phase p and $\mathcal{A}^p$ refers to the set of dislocations whose core is located within the phase p. The whole computational domain is denoted by Ω, while Ω_k^m is the region occupied by platelet k. The transformation tensor ε_k^{tr} in each platelet k is determined from the theory of martensitic transformations [9, 10] and consists of an expansion of magnitude δ in the direction normal to nominal the habit plane (interface between austenite and martensite) and a simple shear of magnitude γ parallel to the habit plane. The complementary fields satisfy the following relations:

$$\boldsymbol{\sigma}^c = \mathbb{C}^p \varepsilon^c + \boldsymbol{P}^p \qquad \text{in } \Omega^p , \qquad (4)$$

where Ω^p is the region occupied by phase $p = $ f, a, m and $\varepsilon^c = \frac{1}{2}(\nabla \boldsymbol{u}^c + (\nabla \boldsymbol{u}^c)^T)$. In (4), the tensors $\boldsymbol{P}^p$ are polarization stresses that stem from the difference in elastic properties between the ferrite, austenite and martensite phases, i.e. these tensors take into account inhomogeneities that are ignored in the analytical solutions of the transformation and dislocation problems. Detailed forms for these tensors can be found in [4].

While this decomposition is general, the computations reported on here are for plane strain problems. Assuming that the stress state at time t is known, evolution relations are used to update the number and location of martensitic platelets and dislocations from time t to time $t + \delta t$. The appearance of new dislocation dipoles and martensitic platelets is simulated using sources randomly distributed across the specimen (dislocation sources in ferrite and austenite, and transformation sources in austenite). The nucleation of martensite is based on

the possibility of an embryonic elliptical martensitic platelet (of given aspect ratio e and major semi-axis of length c_0) to grow (see [8] for details). Subsequent growth of a martensitic platelet k is assumed to occur by lateral movement of the tips of the elliptical cross section according to a kinetic law that relates the velocity $v_k^{(q)}$ of tip $q = 1, 2$ to an effective transformation driving force $\bar{f}_k^{(q)}$ as

$$v_k^{(q)} = \frac{\bar{f}_k^{(q)}}{B_{\mathrm{m}}\,(\pi e c)}\,, \qquad 0 \leqslant v_k^{(q)} \leqslant v_{\max}^{\mathrm{m}} \qquad (q = 1, 2), \qquad (5)$$

where B_{m} is a drag coefficient for transformation, c is the current length of the major semi-axis and the tip velocity is limited by a cut-off value $v_{\max}^{\mathrm{m}}$ (see [8] for details and additional rules to handle special situations). Similarly, as proposed in [11], nucleation of dislocation dipoles is modeled by two-dimensional Frank–Read sources whenever the Peach–Koehler force f_i^{d} (driving force for plasticity computed at a dislocation source) exceeds a critical value $f^{\mathrm{cr}} = b\tau^{\mathrm{cr}}$ during a prescribed time interval t_{nuc}, with τ^{cr} the strength of the dislocation source (b is the magnitude of the Burgers vector). Subsequent movement of a dislocation i is determined by its core velocity v_i^{d}, which is specified using the plastic kinetic relation

$$v_i^{\mathrm{d}} = \frac{f_i^{\mathrm{d}}}{B_{\mathrm{d}}}, \qquad 0 \leqslant v_i^{\mathrm{d}} \leqslant v_{\max}^{\mathrm{d}}, \qquad (6)$$

where f_i^{d} is the Peach–Koehler force computed at the core of dislocation i, B_{d} is the drag coefficient for dislocation glide and $v_{\max}^{\mathrm{d}}$ is a cut-off value for the dislocation velocity (additional details can be found in [11]). The discrete dislocation models used for the bcc ferrite and the fcc austenite are formally the same; only the material parameters and the slip systems are different. The behavior of the martensite is mostly elastic until fracture (see [12]), hence no dislocation sources are assigned to the martensitic phase. Dislocations and dislocation sources originally in an austenitic region that transforms into martensite are deactivated (see [8] for details). Grain boundaries are modeled as impenetrable barriers for the movement of dislocations and for the growth of martensitic platelets.

3. Model parameters and boundary conditions

In the present plane strain simulations, the ferritic and austenitic grains are taken such that the out-of-plane direction of the specimen coincides with the $[1\,1\,0]_{\mathrm{f}}$ and $[1\,1\,0]_{\mathrm{a}}$ directions of the bcc ferrite and fcc austenite, respectively. Attention is restricted to the movement of edge dislocations whose lines lie in the out-of-plane direction of the specimens. In-plane plastic deformation is modeled through dislocation glide on the $[1\,\bar{1}\,1]_{\mathrm{f}}(\bar{1}\,1\,2)_{\mathrm{f}}$ and $[\bar{1}\,1\,1]_{\mathrm{f}}(1\,\bar{1}\,2)_{\mathrm{f}}$ slip systems in the ferrite and the $[1\,\bar{1}\,2]_{\mathrm{a}}(\bar{1}\,1\,1)_{\mathrm{a}}$ and $[\bar{1}\,1\,2]_{\mathrm{a}}(1\,\bar{1}\,1)_{\mathrm{a}}$ slip systems in the austenite (see [8] for more details). The slip plane normals of the $(\bar{1}\,1\,2)_{\mathrm{f}}$ and $(1\,\bar{1}\,2)_{\mathrm{f}}$ planes and the slip plane normals of the $(\bar{1}\,1\,1)_{\mathrm{a}}$ and $(1\,\bar{1}\,1)_{\mathrm{a}}$ planes form angles of approximately $60°$ between them. For simplicity, the magnitude of the Burgers vector for ferrite and austenite is assumed to be the similar. The actual transformation systems found in an fcc austenite to bct martensite transformation are not compatible with plane strain conditions, but their effect can be mimicked in the present formulation by choosing two distinct in-plane habit plane normal vectors oriented at angles of $40°$ and $80°$ with respect to the austenitic slip plane normals mentioned above [8].

Unless otherwise noted, the model parameters used in all simulations are the same as those presented in [4] and correspond to representative values for a low-alloyed multiphase steel assisted by transformation-induced plasticity. It is worth mentioning that the elastic properties of the ferrite and the austenite are assumed to be equal, $\mathbb{C}^{\mathrm{f}} = \mathbb{C}^{\mathrm{a}}$, and that the stiffness of martensite is taken to be 30% larger than that of austenite (i.e. $\mathbb{C}^{\mathrm{m}} = 1.3\mathbb{C}^{\mathrm{a}}$), in accordance
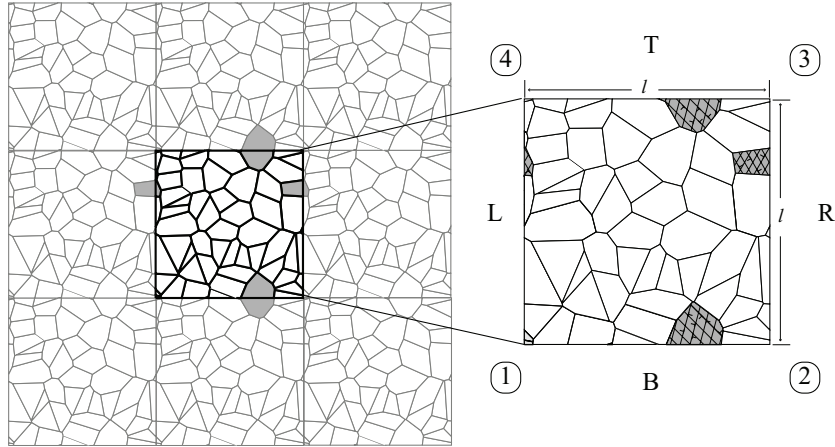
Figure 2. Illustration of a periodic polycrystalline sample.

with the values estimated in [13]. Furthermore, the average dislocation source strength of the ferrite is taken to be 90% of the average strength of the austenite (i.e. the mean values of the Gaussian distributions are such that $\bar{\tau}_f^{cr} = 0.9\bar{\tau}_a^{cr}$ with $\bar{\tau}^{cr} = 150$ MPa and a standard deviation of 30 MPa), which reflects the fact that ferrite is a softer phase in multiphase steels, partly due to its relatively low content of interstitial carbon compared with austenite.

The simulations are carried out using a periodic computational cell consisting of an aggregate of grains of ferrite and (initially) austenitic grains. The polycrystalline samples can be realized by stacking replicas of an $l \times l$ square computational cell in a doubly periodic pattern as shown in figure 2, where the grains are generated using a Voronoi algorithm. In order to ensure periodicity, grains that cross the boundary of the computational cell are viewed as whole grains in the periodic region, vertically and/or horizontally, as indicated in gray color in figure 2. Consequently, slip lines that intersect the boundary need to be extended on the opposite side, vertically and/or horizontally. When a dislocation leaves the primary computational cell, an image dislocation is introduced along the image slip line. For simplicity, configurations are chosen such that austenitic grains do not cross the boundaries of the computational cell, hence image martensitic platelets are trivially avoided. In simulations where austenitic grains intersect the boundary of the unit cell, then the boundary of the unit cell is assigned as a boundary of the austenitic grain.

Periodic displacement are imposed on opposite sides of the cell boundary, i.e., on the left and right sides and on the top and bottom sides, see figure 2. Since the transformation and infinite-space dislocation solutions do not satisfy these periodicity requirements, periodicity is enforced numerically through the complementary problem. In view of (1), the complementary solution is therefore subjected to the kinematic condition

$$u_R^c - u_L^c = (u^{(2)} - u^{(1)}) - (u_R^m - u_L^m) - (u_R^d - u_L^d), \tag{7}$$

$$u_T^c - u_B^c = (u^{(4)} - u^{(1)}) - (u_T^m - u_B^m) - (u_T^d - u_B^d). \tag{8}$$

Here, the subscripts L, R, B and T denote, respectively, points on the left, right, bottom and top boundaries of the computational cell that are pair-wised connected via horizontal and vertical periodicity while $u^{(i)}$ are the displacement vectors of the corner points $i = 1, 2, 4$ as indicated in figure 2.
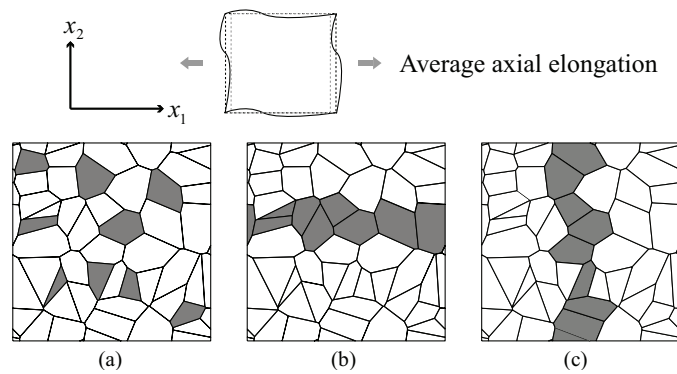
Figure 3. Morphologies of computational samples with (*a*) dispersed austenitic grains (gray), (*b*) horizontally connected austenitic grains and (*c*) vertically connected austenitic grains. Sample (*d*) is the same as (*a*) but the transformation mechanism in the austenitic phase is suppressed. Inset: global coordinate system and sketch of average axial loading for all samples.

4. Simulations

4.1. Geometry and loading of polycrystalline samples

Simulation results are presented in this section to investigate the role of the morphology of retained austenite on the effective response. In particular, samples with approximately the same initial austenitic volume fraction of $\xi_0^A \approx 15\%$ but with different grain connectivities are analyzed. An $8\,\mu\text{m} \times 8\,\mu\text{m}$ cell with uniformly dispersed, isolated grains of austenite embedded in the ferritic matrix is used as the prototypical microstructure of a multiphase steel exhibiting transformation-induced plasticity (see figure 3(*a*)). Two other configurations are considered, as shown in figures 3(*b*) and (*c*), in which all austenitic grains are connected horizontally and vertically, forming a continuous banded (layered) structure. Discontinuous bands of austenitic grains are more representative of low-alloyed multiphase steel since retained austenite has a relatively small volume fraction; nonetheless, for comparative purposes, a continuous band morphology is chosen since the effect of banding can be more clearly established. The purpose of considering the horizontally and vertically connected samples separately is that the effective properties of a banded structure are expected to depend on the relative orientation of loading with respect to the bands. It should be noted, however, that the horizontally and vertically connected cases are not related through a 90° rotation; rather, the two samples have the same grain boundaries and source distributions but the phases are assigned differently. More importantly, the crystal orientation of the individual austenitic and ferritic grains is the same for both the horizontally and vertically connected samples in order to suppress the influence of the crystal orientation that would occur with a 90° rotation (the effect of crystal orientation has been analyzed in [14]). An additional simulation is carried out where the transformation mechanism in the austenitic phase is suppressed in order to establish the relative contribution of the transformation-induced plasticity effect on the overall strength. The configuration for this elasto-plastic simulation is the same as for sample (*a*) and is henceforth referred to as sample (*d*).

In order to minimize the influence of strengthening and/or softening effects other than the spatial distribution of grains, all crystal orientations are kept the same, the specimens are initially dislocation-free and contain no dislocation obstacles except for grain boundaries and the habit planes that appear during the simulation. The slip systems of ferrite and retained
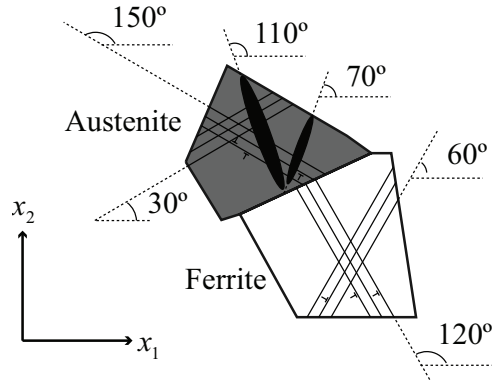
Figure 4. Orientations of slip and transformation systems with respect to the global coordinate system.

austenite and the transformation systems of austenite are symmetrically oriented with respect to the horizontal axis, according to the angles indicated in figure 4. The dislocation source densities are $\rho_{\text{nuc}}^{\text{f}} \approx 88\,\mu\text{m}^{-2}$ and $\rho_{\text{nuc}}^{\text{a}} \approx 30\,\mu\text{m}^{-2}$ for ferrite and austenite, respectively. In all cases, the computational cell is subjected to an average axial deformation in the x_1-direction with an imposed average strain rate of $\dot{\bar{\varepsilon}}_{11} = 10^4\,\text{s}^{-1}$ (specified through the displacement of the corner nodes in the x_1-direction), while the movement of the corner nodes in the x_2-direction is specified so as to mimic an average state of uniaxial tension. The average axial stress $\bar{\sigma}_{11}$ is computed from

$$\bar{\sigma}_{11} = \frac{1}{|\Omega|} \int_{\Omega} \sigma_{11}\mathrm{d}a,$$

where $|\Omega|$ refers to the area of the computational cell Ω.

4.2. Effect of grain connectivity

The evolution of the average axial stress $\bar{\sigma}_{11}$ as a function of the average axial strain $\bar{\varepsilon}_{11}$ is presented in figure 5 for the samples indicated in section 4.1. The transformation-induced plasticity effect can be observed by comparing the response curves of the sample (*a*) with dispersed transforming austenitic grains and sample (*d*) with dispersed grains where the transformation mechanism has been suppressed. Their responses remain similar until $\bar{\varepsilon}_{11} \approx 0.0045$ when the transforming material acquires a higher strength and work-hardening rate than the sample without transformation. This result is in accordance with previous simulations [4] using mixed displacement-traction boundary conditions and confirms that the transformation-induced plasticity effect is also captured in the present simulations where periodic boundary conditions have been applied.

The stress responses for the samples with horizontally and vertically connected austenitic grains are similar to each other for the whole strain range used in the simulations. Despite an early softening, the axial stress for the samples with connected grains eventually rise above the non-transforming sample, which indicates that the transformation-induced plasticity effect in general does increase the strength of the material regardless of the spatial distribution of austenitic grains. The response of the samples with connected grains remains below that of the sample with uniformly dispersed transforming grains, which therefore corresponds to the most favorable morphology in terms of strength. Nonetheless, the hardening rate, measured in
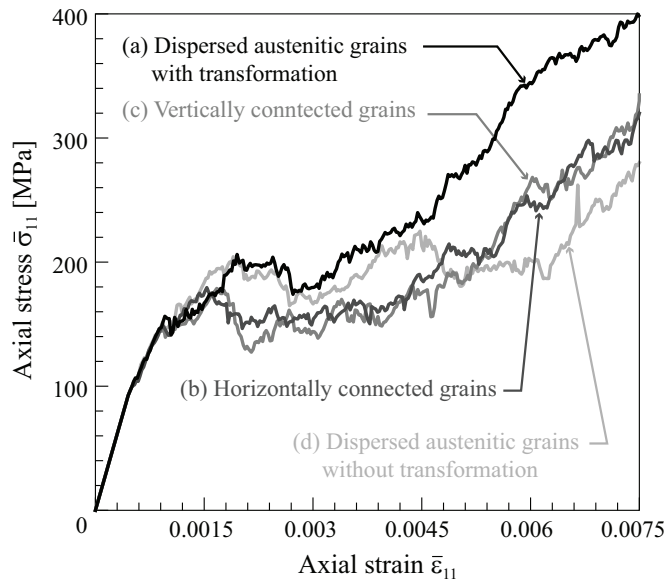
Figure 5. Average axial stress $\bar{\sigma}_{11}$ as a function of the average axial strain $\bar{\varepsilon}_{11}$ for various samples.

terms of the slope of the stress–strain curves, eventually becomes somewhat similar for both dispersed and connected samples.

The above-mentioned features of the stress–strain response curves of the various samples can be traced back to the underlying inelastic mechanisms. The development of the total dislocation density and the volume fraction of austenite as a function of the average axial strain are indicated in figures 6 and 7, respectively. The volume fraction of austenite is normalized with respect to its initial value, i.e. $\bar{\xi}^A = \xi^A/\xi_0^A$.

In terms of the transformation-induced plasticity effect, it can be observed that the point of significant departure between the stress responses of the samples with transforming and non-transforming dispersed austenitic grains, curves (*a*) and (*d*) at $\bar{\varepsilon}_{11} \approx 0.45\%$ as shown in figure 5, coincides with a decrease in the average transformation rate. The decrease in the transformation rate can be inferred from the average slopes of curve (*a*) in figure 7 before and after $\bar{\varepsilon}_{11} \approx 0.45\%$. A decrease in the transformation rate implies that less stress relaxation is available via the transformation mechanism and, consequently, there is an increase in the work-hardening rate.

Despite the similarity of the stress–strain responses of the samples with horizontally and vertically connected austenitic grains (samples (*b*) and (*c*)), their plastic and transformation responses are rather different. Indeed, as can be observed in figure 6, the plastic deformation, measured in terms of total dislocation density, is higher for the sample with vertically connected austenitic grains compared with the sample with horizontally connected grains. Similarly, from figure 7, the deformation associated with transformation, measured in terms of austenitic volume fraction, is higher for the sample with horizontally connected austenitic grains compared with the sample with vertically connected grains. Hence, a similar stress–strain response is achieved for the samples with horizontally and vertically connected austenitic grains by 'compensating' the two inelastic mechanisms.

In order to analyze the effect of grain connectivity in more detail, distributions of the axial stress are shown in figure 8 for a strain level of $\bar{\varepsilon}_{11} = 0.78\%$, i.e. at the end of the response
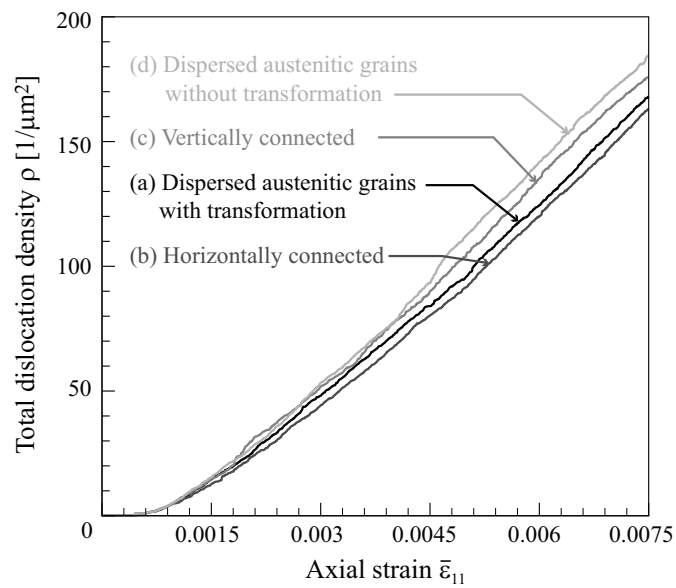
Figure 6. Total dislocation density ρ as a function of the average axial strain $\bar{\varepsilon}_{11}$ for various samples.
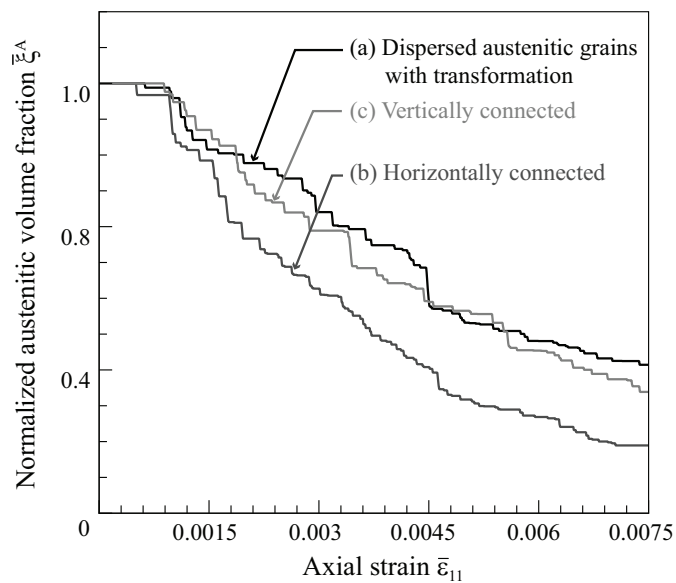
Figure 7. Normalized austenitic volume fraction $\bar{\xi}^A$ as a function of the average axial strain $\bar{\varepsilon}_{11}$ for various samples.

shown in figure 5. The contour plots also reveal the distribution of martensitic platelets, indicated as ellipses inside the austenitic grains. Comparing figure 8(*a*) with the other contour plots, we see that the axial stress for the sample of dispersed transforming austenitic grains is more evenly distributed than for the other samples. The ferritic matrix in the samples with

9
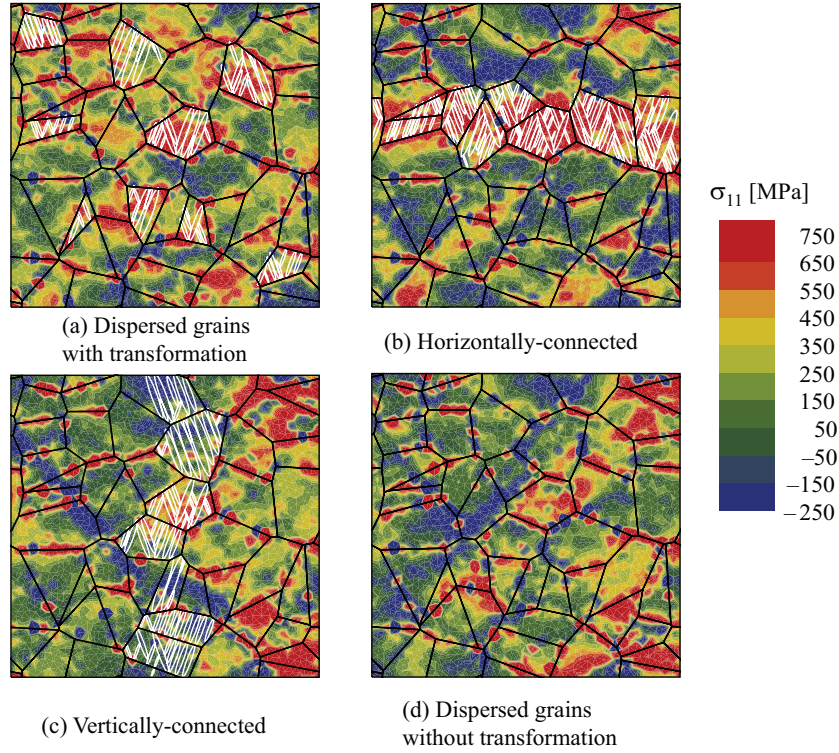
Figure 8. Contour plots of axial stress $\bar{\sigma}_{11}$ and distribution of martensitic platelets of (*a*) dispersed case, (*b*) horizontally connected case, (*c*) vertically connected case and (*d*) dislocation-only case. All contours correspond to an average strain of $\bar{\varepsilon}_{11} = 0.78\%$.

horizontally and vertically connected austenitic grains (samples (*b*) and (*c*)) shows large areas in compression. The same situation is observed in the sample with dispersed, non-transforming grains (sample (*d*)).

Further insight can be obtained by analyzing the spatial distribution of plastic deformation in the various samples. A useful measure for this purpose is an equivalent plastic slip that can be obtained through post-processing of the solution σ and ε given by the discrete method (see (1)). To this end, one can introduce a (continuum) decomposition of the total strain ε as follows:

$$\varepsilon = \varepsilon^{\mathrm{e}} + \varepsilon^{\mathrm{tr}} + \varepsilon^{\mathrm{p}}, \tag{9}$$

where ε^{e}, $\varepsilon^{\mathrm{tr}}$ and ε^{p} correspond to the elastic, transformation and plastic parts. The first two parts are given by

$$\varepsilon^{\mathrm{e}} = \mathbb{D}^{p}\boldsymbol{\sigma}, \qquad \varepsilon^{\mathrm{tr}} = \begin{cases} \mathbf{0} & \text{in } \mathbb{R}^{2} - \Omega_{k}^{\mathrm{m}}, \\ \varepsilon_{k}^{\mathrm{tr}} & \text{in } \Omega_{k}^{\mathrm{m}}, \end{cases} \tag{10}$$

where $\mathbb{D}^{p}$ is the compliance tensor of phase $p = \mathrm{f}, \mathrm{a}$ or m for the ferritic, austenitic or martensitic phases, respectively, and $\varepsilon_{k}^{\mathrm{tr}}$ is the transformation strain associated with the martensitic platelet Ω_{k}^{m}. If a continuum crystal plasticity had been used, the plastic strain could be expressed in terms of the accumulated plastic slip $\gamma^{(\alpha)}$ on the N slip systems by

$$\varepsilon^{\mathrm{p}} = \sum_{\alpha=1}^{N} \gamma^{(\alpha)} \boldsymbol{s}^{(\alpha)} \otimes \boldsymbol{n}^{(\alpha)}, \tag{11}$$
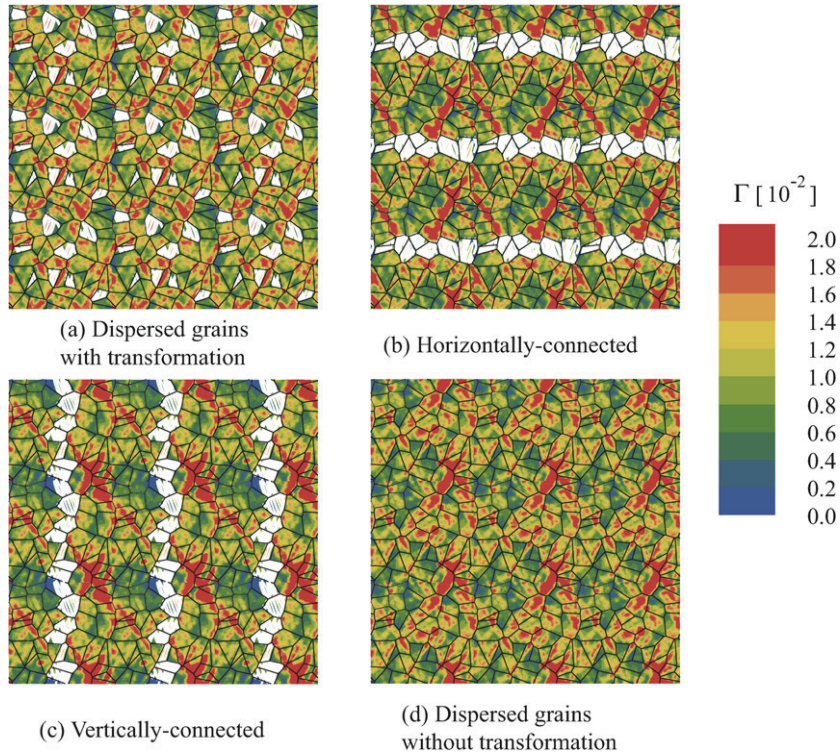
Figure 9. Contour plots of equivalent plastic slip for (*a*) dispersed case, (*b*) horizontally connected case, (*c*) vertically connected case and (*d*) dislocation-only case at an axial strain of $\bar{\varepsilon}_{11} = 0.78\%$.

with $s^{(\alpha)}$ the tangent vector and $n^{(\alpha)}$ the normal vector to slip system $\alpha = 1, \ldots, N$. Here, however, we compute the plastic strain tensor ε^{p} by subtracting the elastic and transformation parts calculated by means of (10) from the total strain, in accordance with (9). Subsequently, it is used to obtain the equivalent plastic slip Γ defined as

$$\Gamma = \sum_{\beta=1}^{N} \left| s^{(\beta)} \cdot \varepsilon^{\mathrm{p}} n^{(\beta)} \right| . \tag{12}$$

Contour plots of the equivalent plastic slip are shown in figure 9 at an axial strain of $\bar{\varepsilon}_{11} = 0.78\%$ for all configurations. To better visualize the distribution of plastic slip, nine adjacent cells are shown for each configuration. As can be observed from the figure, the plastic deformation for the sample with dispersed transforming austenitic grains (figure 9(*a*)) is more evenly distributed than for the other samples. Plastic slip in the horizontally and vertically connected *austenitic* grains is relatively low, while plastic deformation in the corresponding *ferritic* matrices tends to be concentrated in a few areas that, through periodicity of the computational cell, can be interpreted as *slip bands* as shown in figures 9(*b*) and (*c*). Contrary to expectations, the connected austenitic grains (both horizontal and vertical) do not form an effective barrier for plastic slip in the ferrite. In fact, even though the slip bands in the ferrite are confined between the layers of austenitic grains (that have partially transformed to martensite), these slip bands continue in subsequent ferritic layers forming what may be described as a long range slip band. In contrast, as can be observed in figure 9(*a*), the formation of long range slip bands is rather limited in the sample with dispersed transforming austenitic

11

grains. In that case, short range slip bands (spanning one to two ferritic grains) percolate through all grains in the ferritic matrix resulting in a uniform distribution of plastic slip in the ferritic matrix. This uniform distribution of plastic slip may not only be ascribed to the spatial distribution of austenitic grains, but also to their transformation into martensite. Indeed, the sample with dispersed but non-transforming austenitic grains shown in figure 9(*d*) has better defined slip bands than the sample with dispersed transforming austenitic grains shown in figure 9(*a*), which indicates that the transformation mechanism helps to delay plastic localization.

Experimental studies reported in [15, 16] show that a microstructure with uniformly dispersed grains of retained austenite (the so-called granular austenite) performs macroscopically better in terms of strength compared with a microstructure where the retained austenite appears intertwinned in elongated bainitic grains (known as interlath austenite). The difference in performance has been attributed to the fact that interlath austenite hardly transforms into martensite upon mechanical loading whereas the granular austenite does. Despite that the present analysis does not take into account some of the features observed in the experimental studies, the simulations shown here indicate that indeed the transformation mechanism plays a significant role. More importantly, this work shows that the *spatial distribution* of austenitic grains can play an equally relevant role in determining the strength of the material, as demonstrated by the effective responses shown in figure 5.

5. Concluding remarks

The role of the spatial distribution of austenitic grains in a multiphase material has been analyzed by means of computational volumes subjected to periodic boundary conditions. The sample with uniformly dispersed transforming austenitic grains showed the highest strength due to the absence of localized slip bands in the ferritic matrix. In contrast, slip bands formed within the ferritic matrix for samples where the ferrite is confined by connected austenitic grains, effectively reducing the overall strength. In terms of the phase transformation, the highest transformation rate was observed for a morphology where the austenitic layer is aligned with the loading direction. Although more transformation was accompanied with less plastic deformation (measured in terms of number of dislocations), this sample had well-defined slip bands in the ferritic matrix that significantly affected the average strength.

It is likely that localization would inevitably occur in samples with dispersed transforming austenitic grains if the strain level is further increased in the simulations. However, for computational reasons, the analysis is limited to a relatively small strain range, which prevents a numerical validation of this hypothesis. Nevertheless, the present simulations indicate that a microstructure with uniformly distributed transforming austenitic grains delays the onset of plastic localization and has higher strength than a material with a layered microstructure. This observation suggests that banded microstructures in multiphase steels assisted by transformation-induced plasticity are in general detrimental from the point of view of strength.

References

[1] Jacques P J, Ladrière J and Delannay F 2001 On the influence of interactions between phases on the mechanical stability of retained austenite in transformation-induced plasticity multiphase steels *Metall. Mater. Trans.* A **32** 2759–68

[2] Basuki A and Aernoudt E 1999 Influence of rolling of TRIP steel in the intercritical region on the stability of retained austenite *J. Mater. Process. Technol.* **89–90** 37–43

  [3] Verlinden B, Driver J, Samajdar I and Doherty R D 2007 Thermo-mechanical processing of steel *Thermo-Mechanical Processing of Metallic Materials* (*Pergamon Materials Series* vol 11) ed R W Cahn (Oxford: Pergamon) pp 405–48
  [4] Shi J, Turteltaub S and Van Der Giessen E 2010 Analysis of grain size effects on transformation-induced plasticity based on a discrete dislocation-transformation model *J. Mech. Phys. Solids* **58** 1863–78
  [5] Grange R A 1971 Effect of microstructural banding in steel *Metall. Trans.* **2** 417–26
  [6] Charles J A 1998 Development and use of layered ferrous microstructure *Mater. Sci. Technol.* **14** 496–503
  [7] Tasan C C, Hoefnagels J P M and Geers M G D 2010 Microstructural banding effects clarified through micrographic digital image correlation *Scr. Mater.* **62** 835–8
  [8] Shi J, Turteltaub S, Van der Giessen E and Remmers J J C 2008 A discrete dislocation–transformation model for austenitic single crystals *Modelling Simul. Mater. Sci. Eng.* **16** 055005
  [9] Wechsler M S, Lieberman D E and Read T A 1953 On the theory of the formation of martensite *Appl. Phys.* A **197** 1503–15
 [10] Ball J M and James R D 1987 Fine phase mixtures as minimizers of energy *Arch. Ration. Mech. Anal.* **100** 13–52
 [11] Van der Giessen E and Needleman A 1995 Discrete dislocation plasiticity: a simple planar model *Modelling Simul. Mater. Sci. Eng.* **3** 689–735
 [12] Jacques P J, Furnémont Q, Godet S, Pardoen T, Conlon K T and Delannay F 2006 Micromechanical characterisation of TRIP-assisted multiphase steels by in situ neutron diffraction *Phil. Mag.* **86** 2371–92
 [13] Turteltaub S and Suiker A S J 2005 Transformation-induced plasticity in ferrous alloys *J. Mech. Phys. Solids* **53** 1747–88
 [14] Shi J, Turteltaub S and Van der Giessen E 2009 Effect of austenitic crystal orientation in a multiphase steel analyzed by a discrete dislocation-transformation model *Proc. 12th ESAFORM Conf. on Material Forming (Enschede, Netherlands)* ed A H van den Boogaard and R Akkermann *Int. J. Mater. Forming (Suppl 1)* **2** 435–8
 [15] Koh H J, Lee S K, Park S H, Choi S J, Kwon S J and Kim N J 1998 Effect of hot rolling conditions on the microstructure and mechanical properties of Fe–C–Mn–Si multiphase steels *Scr. Mater.* **38** 763–8
 [16] Lee H, Koh H J, Seo C-H and Kim N J 2008 Microstructure and tensile properties of hot-rolled Fe–C–Mn–Si–Cu multiphase steel *Scr. Mater.* **59** 83–6